Calculating centrality variables and geometric quantities for Pb+Pb and Au+Au collisions using a Monte Carlo Glauber model

Anya Wolterman*
Department of Physics and Astronomy, Macalester College

Advisor: Professor Manuel Calderón de la Barca Sánchez[†]
Department of Physics, University of California Davis

The Glauber model provides insight into the initial state of nuclear collisions by treating them in terms of the interactions of their constituent nucleons, in accordance with theories about the scattering of composite particles. These phenomenological techniques are commonly used to determine various geometric quantities associated with such femtoscopic many-body systems. The Monte Carlo Glauber approach uses a random impact parameter and measured nuclear densities to investigate quantifiable properties such as the particle multiplicity and the average geometric eccentricity for heavy ion collisions. The former involves the incorporation of a particle production model to plot the total transverse energy or the number of particles produced at midrapidity, both being measures of centrality. The latter delves into the eccentricity of different event classes, which can be used to characterize various collision shapes for measurements of elliptic flow of heavy mesons. The results of both applications are then compared with analyses of data from the CMS and STAR experiments as part of efforts to study the properties of the ultrahot, super-dense phase of matter known as the Quark-Gluon Plasma.

I. INTRODUCTION

High energy physics seeks to further our understanding of the fundamental nature of matter, from the familiar world of electromagnetically-interacting electrons and nucleons to a more exotic phase of matter thought to have existed only microseconds after the Big Bang. One of these highly sought after and studied states is known as the Quark-Gluon Plasma (QGP), in which baryonic matter exists as a hot, dense mixture of quarks and gluons, collectively known as partons. These partons are believed to have occupied this color-deconfined state within the first 10^{-6} to 10^{-5} seconds of the universe's existence, at a temperature still above 10^{12} K, just prior to coalescing into more familiar hadronic matter.

In order to recreate the extreme conditions of this early state, particle colliders like the LHC and RHIC accelerate heavy atomic nuclei to ultra-relativistic speeds in order to squeeze the highest possible energies into the smallest possible volume [1]. The resulting violent collisions melt the nucleons, transforming the confined quarks (held within hadrons due to the asymptotic freedom property of the strong force) into a quasi-free QGP state. On the order of 10^{-23} seconds later, the quarks, antiquarks, and gluons created from the available energy recombine into hundreds of hadrons that explode outward into the detectors. Understanding the bulk and transport properties of the QGP and the phase transition to this color-deconfined state first requires a better comprehension of the theory regarding the fundamental force governing the QGP: quantum chromodynamics.

A. Quantum chromodynamics

Protons and neutrons are each composed of three valence quarks, which are kept confined within each nucleon by the strong nuclear force, an interaction described by quantum chromodynamics (QCD). QCD is one of the three quantum field theories that make up the Standard Model of fundamental interactions among elementary particles; the other two are quantum electrodynamics for the electromagnetic force, and quantum flavordynamics for the weak nuclear force. Interestingly, most of the baryonic mass in the universe actually comes from QCD. The Higgs mechanism is responsible for the mass of the quarks (and the electrons) themselves, but that is only 1% of the total nucleon mass, meaning the remaining 99% comes from the strong interactions between the quarks [2]. Furthermore, nucleons comprise most of the mass of the atom and thus QCD is responsible for the majority of everyday mass. Understanding the behavior of this force at high energies could contribute to a better understanding of nuclear matter in general.

The strong force is mediated by eight neutral gluons, which are massless spin-1 bosons that are self-interacting because they can carry color and anti-color charge themselves. Color charge is analogous to electric charge, except for the fact that it is not static; quarks can change color because the gluons they exchange carry color charge themselves, while an electron will always be negatively-charged since the QED mediator, the photon, carries no electric charge. There are three color charges—red, green, blue—and their respective anticolors, with neutral "white" combinations being made as either color plus anticolor or as three different colors or anticolors.

One of the most unusual aspects of QCD is the phenomenon of asymptotic freedom, a product of gluon self-

_____

* awolterm@macalester.edu
† http://www.nuclear.ucdavis.edu/~calderon/

coupling in which the strong force increases as the distance between the color-charged objects grows; this is entirely contrary to the familiar behavior of the electromagnetic and gravitational forces, which drop off in strength as the distance between the interacting objects increases. High energies, and therefore short distances, are sought out since the coupling constant shrinks in this limit. This bizarre property, which requires a non-Abelian gauge theory to be described, complicates the study of QCD matter like the QGP [3].

B. Quark-Gluon Plasma

In those first few microseconds of the universe (the "primordial universe" shown in Fig. 1), the quarks and gluons that make up ordinary nuclear matter existed as this interesting, strongly-interacting yet deconfined phase. The high temperatures and densities allow the partons to be asymptotically free. Given the timescale of its proposed existence, studying the QGP provides insights into the properties of the very early universe. One of the key difficulties that arises when trying to study the QGP is the previously mentioned phenomenon of confinement and asymptotic freedom. As one tries to separate the quarks, the system reaches a point where it becomes energetically favorable to create a new quark-antiquark pair out of the vacuum, which can then recombine with the escaping quark to make a new hadron. Given that behavior, free solitary quarks have never been observed, and the closest that can be achieved is this quasi-free QGP state. The QGP is called a "plasma" because it was expected to behave like an ultrahot weakly-coupled gas of charged particles. However, experiments have found that it acts more like a strongly-coupled liquid—a perfect fluid exhibiting collective flow with almost no viscosity. The best parameter to describe the observed system is one typically used for liquids: the ratio of shear viscosity to entropy density, η/s. This quantity was found to be nearly zero, making this substance one of the first experimentally accessible perfect liquids ever isolated in a lab, but also suggesting that a true QGP has not formed [4].
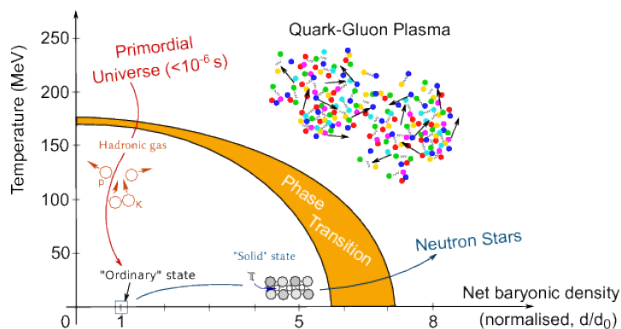

FIG. 1. Phase diagram of QCD matter, showing the transition at $T_c = 150 - 190$ MeV from ordinary confined matter to a deconfined QGP state (source: ALICE Collaboration).

1. Experimental evidence of QGP

There are three pillars of evidence for QGP formation in experimental settings: heavy quarkonium suppression, jet production and quenching, and elliptic flow.

a. Quarkonium suppression Extreme color fields created inside the plasma can screen heavy quarkonia, which are mesons formed from heavy quark-antiquarks pairs. Screening causes the valence quarks to dissociate and form open heavy flavor mesons before the quarkonium can escape the QGP and undergo standard decay in the surrounding vacuum (which would produce detectable signatures) [2]. As the QGP gets hotter, the free partons can screen at smaller and smaller distances, though at any temperature, the weakly-bound quarkonia will be more suppressed than the tightly-bound quarkonia. Thus, measuring suppression of different quarkonia points to the length scale at which the QGP starts to screen, which in turn informs about the temperature [5].

b. Jet quenching A key aspect of QCD, the production of jets involves the high-momentum scattering of quarks and gluons that produces narrow, back-to-back sprays of hadrons. Head-on collisions between partons generate bursts of energy that quickly condense into "jets" of pions, kaons, and other particles. These jets are formed in pairs, one of which gets weakened or extinguished if it has to traverse the dense fireball produced in a heavy ion collision, experiencing significant energy loss due to interactions with the quark- and gluon-rich medium. The jets are considered hard probes in that they are strongly interacting but moving fast enough not to be completely absorbed by the medium. The amount of quenching, the orientation and composition of the jets, and the manner in which the jets transfer energy and momentum all reveal information about the contents of the fireball and therefore the properties of the QGP [6].
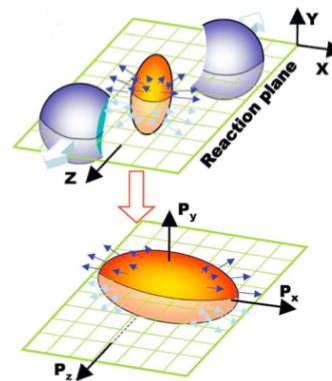

FIG. 2. Geometry of a non-central heavy ion collision. The spherical approximations for the colliding nuclei do not account for the highly relativistic speeds at which the collisions are occurring (i.e. should have more flattened cross sections).

c. Elliptic flow An important feature of a hot, dense, strongly-coupled QGP is the azimuthal anisotropy

of emitted charged particles. Non-central nuclear collisions produce an almond-shaped overlap region, as shown in Fig. 2. The strong rescattering of partons in the initial state of the collision leads to the formation of local thermal equilibria, which in turn causes the buildup of non-uniform pressure gradients in the almond. This drives anisotropic expansion of the plasma such that outgoing particles are emitted preferentially along the direction of the impact parameter vector between the two nuclei. Flow has final state observables (e.g. pions formed late in the evolution), but the momentum distribution preserves information from early in the collision because of its intrinsic connection with the initial spatial anisotropy. The medium's high opacity and the elliptical distribution of emitted hadrons are both more characteristic of a fluid; if the QGP behaved like a gas, the hadrons would emerge uniformly in all directions from a less opaque plasma. Continuing to study flow in this system, especially elliptic flow, will provide more insight into the QGP's bulk properties (e.g. viscosity, equation of state) [2].

C. Experimental facilities

The aforementioned signatures of QGP formation are studied at the Large Hadron Collider and at Brookhaven National Lab's Relativistic Heavy Ion Collider, within the Compact Muon Solenoid (CMS) and the Solenoidal Tracker at RHIC (STAR) experiments, respectively; other experiments at these colliders focus on other pressing physics questions. In both general purpose detectors, violent collisions between highly relativistic heavy nuclei generate femtoscopic fireballs of melted nucleons that can send hundreds of particles flying out into the surrounding trackers and calorimeters. In particular, these experiments rely on lead and gold nuclei, which are capable of reaching the extreme pressure and temperature conditions needed to create a QGP thanks to their relatively high densities.

1. Compact Muon Solenoid

One of two general purpose detectors at the LHC, the CMS experiment is pursuing a broad range of physics questions, from the Standard Model and the Higgs boson, to searches for extra dimensions and dark matter candidates. Following a high energy collision of two heavy nuclei in the heart of the detector, the innermost silicon trackers first reconstruct the paths of the charged particles coming out of the high energy collision. Next, the two calorimeters measure the energy of the outgoing particles; the electromagnetic calorimeter measures electrons and photons using $PbWO_4$ crystals, while the hadron calorimeter detects any particle made of quarks or gluons. The previous parts are enclosed in a superconducting solenoid that generates a 3.8 T magnetic field. Lastly, the iron magnet return yoke stops all remaining particles

from reaching the expansive muon chambers dedicated to stopping the very weakly interacting muons.

2. Solenoidal Tracker At RHIC

While CMS investigates a variety of scientific inquiries, STAR is designed to focus on the formation and behavior of high-density, strongly-interacting matter. STAR is schematically similar to CMS in its concentric arrangement of trackers (silicon and gaseous), an electromagnetic calorimeter, and a solenoidal magnet around the beam interaction region. The heart of STAR is the Time Projection Chamber (TPC), which serves as the primary tracking device, measuring particles' tracks, momenta, and ionization energy loss [7]. The TPC is surrounded by the Time Of Flight detector, which measures the time of flight that can then be used with the corresponding transverse momentum to identify particles. These are all contained within a solenoidal magnet operating at 0.5 T.

II. THE GLAUBER MODEL

Given the complexity of heavy ion collisions, it is natural to wonder about the number of incident nucleons that actually participate in a particular interaction and the shape of the overlap between the nuclei. The phenomenological techniques that have been developed to figure out these quantities for these types of femtoscopic many-body systems are known as Glauber models.
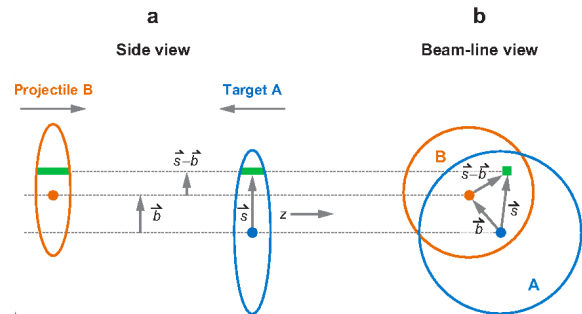

FIG. 3. Schematic of a collision between two nuclei, with the offset between their two centers being represented by the impact parameter vector b.

The Glauber model treats collisions between nuclei as independent sequences of individual nucleon-nucleon interactions, getting its theoretical basis from quantum theories about scattering of composite particles [8]. Since the femtometer scales on which these collisions occur precludes direct observation, the impact parameter (a vector b representing the offset between the centers of the two nuclei, see Fig. 3), the number of nucleons that experience at least one nucleon-nucleon collision (number of "participants", N_{part}), and the number of binary nucleon-nucleon collisions (N_{coll}) all must be estimated

from experimental data using these theoretical methods. Together with the impact parameter b, the quantities N_{part} and N_{coll} characterize the centrality of the collision—i.e. its size, shape, and degree of overlap between the incident nuclei at the interaction point.

For a Monte Carlo Glauber (MCG) model, the only required inputs are a randomly generated impact parameter, a measured nuclear density function $\rho(r)$, and a measured inelastic nucleon-nucleon cross-section $\sigma_{\text{inel}}^{\text{NN}}$ [9]. This last parameter is calculated as the total nucleon-nucleon cross-section minus the elastic nucleon-nucleon cross-section, both of which are experimentally measurable quantities. The focus is on inelastic collisions because those actually produce new particles, as opposed to elastic collisions in which the nucleons simply scatter off each other without fragmenting. The specific value of $\sigma_{\text{inel}}^{\text{NN}}$ essentially relates to how big a nucleon is, which in turn depends on its energy in that higher center-of-mass energies are associated with larger cross-sections; this could be due to the stronger interactions that occur as the mass and charge of the nucleus is further concentrated/condensed at higher energies. It is used to determine how close the nucleon trajectories need to be in order for a collision to occur. Since it is based purely on nuclear geometry, this type of modeling is fairly simple and does make some fundamental assumptions. Here, the nucleons are assumed to follow straight line trajectories, and $\sigma_{\text{NN}}^{\text{inel}}$ is taken to be independent of any previous collisions, and therefore the nuclei are modelled as just passing through each other.

A. Woods-Saxon nuclear density function

The only input values that must be known prior to constructing and utilizing an MCG model are $\sigma_{\text{NN}}^{\text{inel}}$ and the parameters for the nuclear density function, in this case the Woods-Saxon equation in Fig. 4.
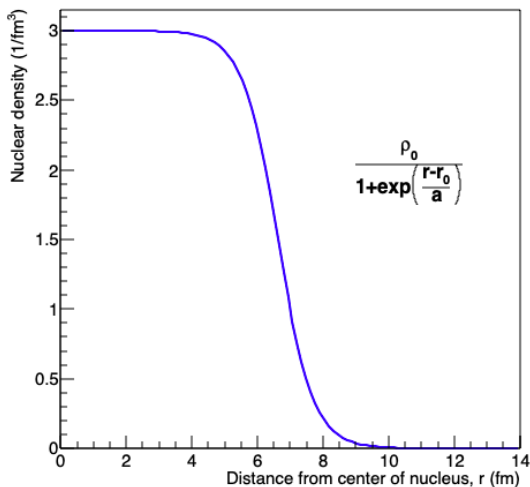

FIG. 4. Radial density function for a Pb nucleus ($r_0 = 6.62$ fm, $a = 0.542$ fm) assuming a Woods-Saxon distribution.

The Woods-Saxon function governs the density of nucleons as a function of distance from the center of the nucleus, where ρ_0 is the nuclear density at the center, r_0 is the nuclear radius, and a is the skin depth (which characterizes how sharp the edge of the nucleus is). The Woods-Saxon distribution becomes a step function in the hard sphere limit (as a goes to zero) since the nucleus is now being treated as a sphere-shaped object with well-defined, and not diffuse, boundaries.

The radial probability function is calculated by multiplying the Woods-Saxon function by r^2. This equation is then used to randomly distribute the nucleons that will be accelerated towards each other in any given run of the model. The x, y, and z coordinates for each of the 416 nucleons in Pb+Pb, or all 394 in Au+Au, are randomly determined according to a $\rho(r) * r^2$ like in Fig. 5.
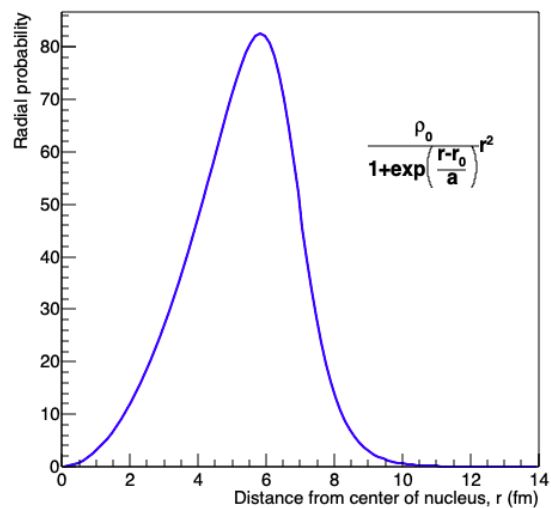

FIG. 5. Radial probability function for a Pb nucleus.

B. Impact parameter generation

After the nucleons in the simulation have been randomly distributed in accordance with the Woods-Saxon function, all of the constituents of one nucleus are shifted laterally by the impact parameter. A specific value of b is drawn from the distribution

$$\frac{d\sigma}{db} = 2\pi b\,,$$

indicating that the probability of a given impact parameter follows a linear trend. Selecting an impact parameter is analogous to trying to hit a bullseye, in that the target area is proportional to the probability. Thus, the probability of a head-on, central collision ($b = 0$) is much lower than probability of a more peripheral collision (large b). In reality, the impact parameter vector can point in any direction because of the assumed spherical symmetry of the system, but for convenience the offset is taken to be in the $+x$ direction in this model.

In order for any two nucleons to experience a binary collision, the following condition for the distance d between them must be satisfied:

$$d \leq \sqrt{\sigma_{\text{inel}}^{\text{NN}}/\pi}\,.$$

For a collision between nucleus A and nucleus B, every nucleon in A is checked against every nucleon in B to determine if their randomly generated coordinates will lead to a binary nucleon-nucleon collision. Every nucleon that experiences at least one binary collision is marked by a darker color in Fig. 6 to distinguish it from the spectator nucleons. Note the almond-shaped overlap region visible from this z-direction (beam-line) view; the particles emitted along the short axis of the almond will experience the greatest momentum boost.
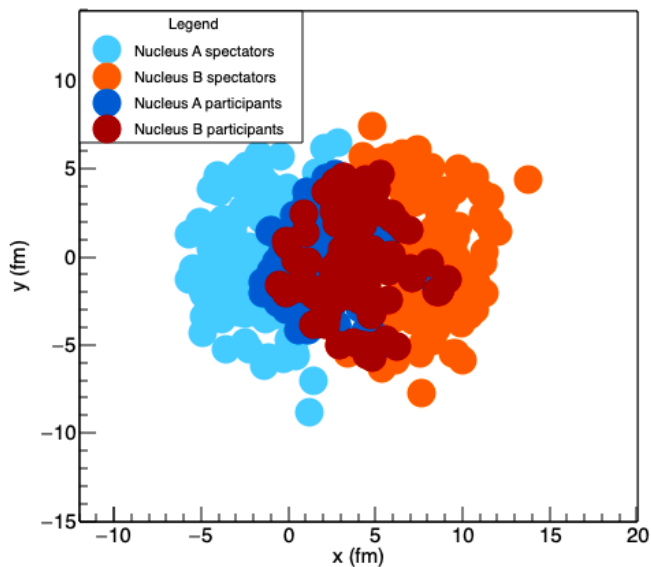

FIG. 6. Distribution of all 416 nucleons for a Pb+Pb collision at $\sqrt{s_{\text{NN}}} = 2.76$ TeV with $\sigma_{\text{inel}}^{\text{NN}} = 65$ mb and $b = 6$ fm.

C. Resulting histograms and correlations

After running 10^6 pseudo-experiments of the model, about 75% of which resulted in at least one binary nucleon-nucleon collision, the following distributions of b, N_{part}, and N_{coll} were generated. The impact parameter histogram (Fig. 7) shows the number of counts of b increases linearly with the value of b itself (as expected given the manner in which b was generated) up until about twice the nuclear radius, at which point the probability of any nucleon-nucleon collisions starts to drop off. However, it is not a sharp drop off because the nuclei are not hard spheres, but instead are a bit more diffuse (as seen in the nucleon distribution plot in Fig. 6). The N_{part} histogram (Fig. 8) does have a sharp drop off since there is a well-defined maximum number of participants (416 for Pb+Pb, 394 for Au+Au). Lastly, the N_{coll} histogram (Fig. 9) exhibits a characteristic horseback shape.
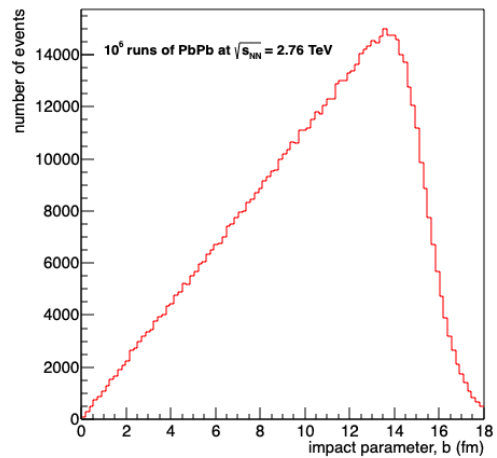

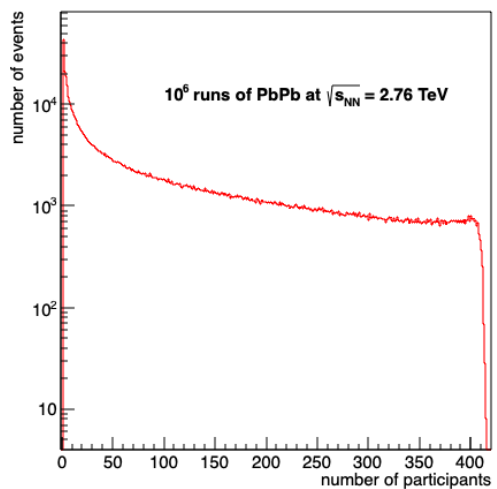FIG. 7. Histogram of impact parameter values for the trials that resulted in at least one nucleon-nucleon collision.

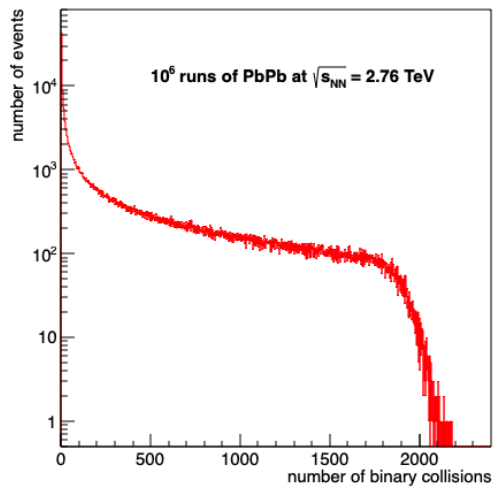FIG. 8. Histogram of resulting N_{part} for events with $N_{\text{coll}} \geq 1$.

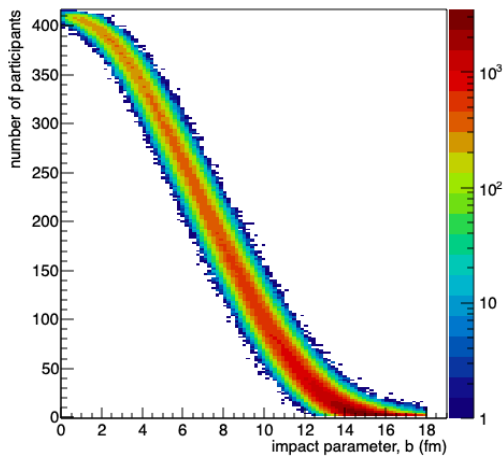FIG. 9. Histogram of resulting N_{coll} for events with $N_{\text{coll}} \geq 1$.

FIG. 10. Correlation between N_{part} and b.

As expected, there is a positive correlation between N_{part} and N_{coll}, since a greater number of interacting nucleons would logically be associated with a greater number of nucleon-nucleon collisions occurring. There is a clear negative correlation between the impact parameter and both N_{part} (shown in Fig. 10) and N_{coll}; a smaller impact parameter corresponds to a more central collision that sees higher numbers of participants and binary collisions due to the increased overlap between the nuclei. In the correlation plot, one can clearly see a hot spot (i.e. the most probable outcome of a run, the dark red portion of Fig. 10) at high b, low N_{part}, and low N_{coll}.

None of the variables noted previously—b, N_{part}, or N_{coll}—can be measured experimentally, so in order to more directly compare the model against experimental data, a particle production model must be incorporated into the existing MCG simulation. This step involves the calculation of a centrality variable using a negative binomial distribution (NBD).

D. Particle production model and the negative binomial distribution

Centrality variables are measurable quantities that relate to how head-on a given nucleus-nucleus collision is. CMS uses the total transverse energy ΣE_{T}, while STAR uses the particle multiplicity $dN_{ch}/d\eta$ at mid-rapidity (around $\eta = 0$, about $\pm 30°$ from perpendicular to the beam line). In a detector, these are measured as tracks in the trackers (for the multiplicity) or as energy deposited in the calorimeters (for ΣE_{T}). Both are calculated using an NBD, expressed in terms of parameters μ and k using gamma functions as

$$\frac{\Gamma(k+n)}{k!\,\Gamma(n)} \cdot \frac{(\mu/k)^n}{(1+\mu/k)^{n+k}} \,,$$

where n represents the amount of E_{T} or the number of particles produced in a particular nucleon-nucleon collision, μ is the mean E_{T} or multiplicity, and k is a parameter relating to the width of the distribution [9]. The total transverse energy or multiplicity distribution is obtained by convolving the NBD with the N_{coll} histogram.

In both cases, a value is randomly drawn from the NBD to determine the amount of transverse energy or the number of particles produced in one nucleon-nucleon collision. This random drawing is repeated N_{coll} times and summed to calculate the ΣE_{T} or total $dN_{ch}/d\eta$ for a particular nucleus-nucleus collision that had exactly N_{coll} nucleon-nucleon collisions. That entire process is then repeated for however many events out of the 10^6 pseudo-experiments had that specific N_{coll}. Once those calculations have been completed, the generated ΣE_{T} or $dN_{ch}/d\eta$ distribution can be compared with and fit to experimental data by optimizing the NBD parameters.

E. Parameter fitting

For Pb+Pb at $\sqrt{s_{\mathrm{NN}}} = 2.76$ TeV, the best values of μ, k, and the normalization factor were determined by minimizing χ^2 between the generated and experimental ΣE_{T} distributions. A measure of how good a fit is, χ^2 is calculated by summing up $(O - E)^2/E$ for all points, where O is the observed (generated) value and E is the expected (experimental) value of ΣE_{T}. The data were only fit for 0.5-5 TeV, instead of the full 0-5 TeV range, to avoid the inefficiencies of the most peripheral collisions. First, the χ^2 values were calculated in a coarse pass over a range of μ and k. Then, the scaling of the generated ΣE_{T} histogram was varied to find the best value of the normalization factor. This was followed by a finer re-scanning of the μ and k parameter space to find a local minimum in χ^2. The goal of the parameter fitting was to reach a χ^2 around 100, since the system has 98 degrees of freedom from 100 bins in the histogram of the centrality variable minus two parameters. This was achieved in the final scan, shown in Fig. 11, pointing to $\mu = 1.39$, $k = 0.45$, and norm= 0.041 as the values that best match the generated distribution to the CMS data.
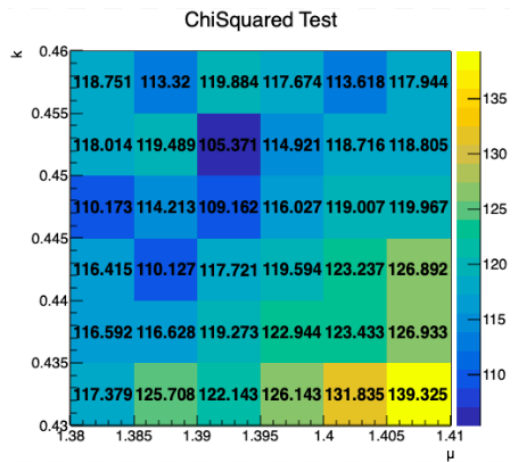

FIG. 11. Final scan of the μ and k parameter space.

F. Determining centrality classes

Calculations of centrality variables are used to create centrality classes, which divide up the results of a particular collision type into fractions of the total integral of the centrality variable distribution. The convention is that 0% represents the most central collision and 100% corresponds to the most peripheral. Cuts are made in the total transverse energy (for Pb+Pb data from CMS) or in the particle multiplicity (for Au+Au data from STAR) to divide the integral in 5% increments, and the ranges corresponding to each percentile are noted so average values of other variables (like N_{part}) as a function of centrality can be determined. Fig. 12 shows the generated ΣE_{T} histogram using the final NBD parameters (listed in the previous section) in comparison with CMS data for Pb+Pb at $\sqrt{s_{\text{NN}}} = 2.76$ TeV. The centrality classes from 0% to 70% based on cuts in ΣE_{T} are marked by the green dashed lines, shown for the 0% to 50% classes in 5% increments, then in 10% increments for the remainder.
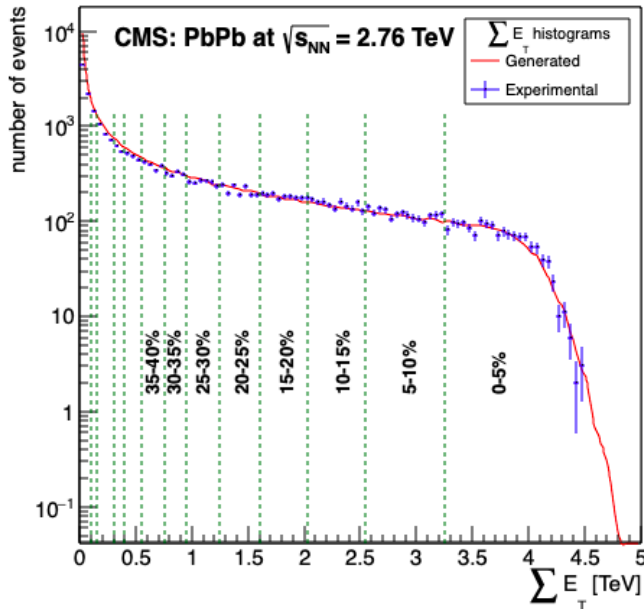

FIG. 12. Final ΣE_{T} histogram for Pb+Pb at 2.76 TeV (red line) with centrality classes (green dashed lines) and CMS data for comparison (blue points with error bars) [10].

III. ECCENTRICITY AND OVERLAP AREA

Both the eccentricity ϵ and overlap area S characterize the almond-shaped overlap region in the initial state of the collision, which is irregular, determined by the impact parameter, and whose orientation fluctuates from event to event. The eccentricity in particular quantifies the initial spatial anisotropy that ultimately results in the anisotropic final momentum distribution for the emitted particles seen in elliptic flow.
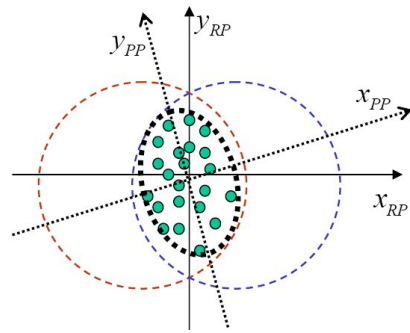

FIG. 13. Reaction plane vs. participant plane.

Both geometric quantities are defined in two coordinate systems, shown in Fig. 13: the reaction plane (determined by the beam direction and the impact parameter vector); and the participant plane (determined by the beam direction and a rotated $x'y'$ frame that aligns itself with the participants. The planes are different because the spatial distribution of participating nucleons is not necessarily symmetric with respect to the reaction plane. Furthermore, the true reaction plane cannot be known experimentally, which is why the participant eccentricity is used more often. This difference translates into the following equations, where the participant version has an extra covariance term in it that rotates the coordinate system depending on the locations of the participants:

$$\epsilon_{\text{RP}} = \frac{\sigma_y^2 - \sigma_x^2}{\sigma_y^2 + \sigma_x^2}, \quad \epsilon_{\text{part}} = \frac{\sqrt{(\sigma_y^2 - \sigma_x^2)^2 + 4\sigma_{xy}^2}}{\sigma_y^2 + \sigma_x^2}$$

$$S_{\text{RP}} = \pi\sqrt{\sigma_x^2 \sigma_y^2}, \quad S_{\text{part}} = \pi\sqrt{\sigma_x^2 \sigma_y^2 - \sigma_{xy}^2}$$

in which the variances and the covariance are calculated as $\sigma_x^2 = <x^2> - <x>^2$, $\sigma_y^2 = <y^2> - <y>^2$, and $\sigma_{xy} = <xy> - <x><y>$ [11]. By definition, ϵ_{part} can only have positive values and represents the maximum calculated eccentricity for a given collision regardless of the direction of the initial b vector.

IV. RESULTS

A. Au+Au at $\sqrt{s_{\text{NN}}}$ = 200 GeV

For my initial calculations of ϵ and S, I switched from Pb+Pb at $\sqrt{s_{\text{NN}}} = 2.76$ TeV to Au+Au at $\sqrt{s_{\text{NN}}} = 200$ GeV since the paper in which I had found the relevant equations focused on that type of heavy ion collision [11]. The behavior of the average reaction-plane and participant eccentricities as functions of the average number of participants was found to be consistent with expectations from published plots, with Fig. 14 showing this expected behavior. The monotonic trend observed for the average ϵ_{part} is not seen with ϵ_{RP}; the drop-off occurs because

for very peripheral collisions (low N_{part}) there are larger fluctuations in the shape and orientation of the already small nuclear overlap and rotating the coordinate system to better line up with the participants counteracts that. Additionally, note that at high numbers of participants, the two coordinate systems and calculation methods for ϵ are more consistent with each other than in the low N_{part} case—another example of the generally higher discrepancy/uncertainty associated with peripheral collisions.
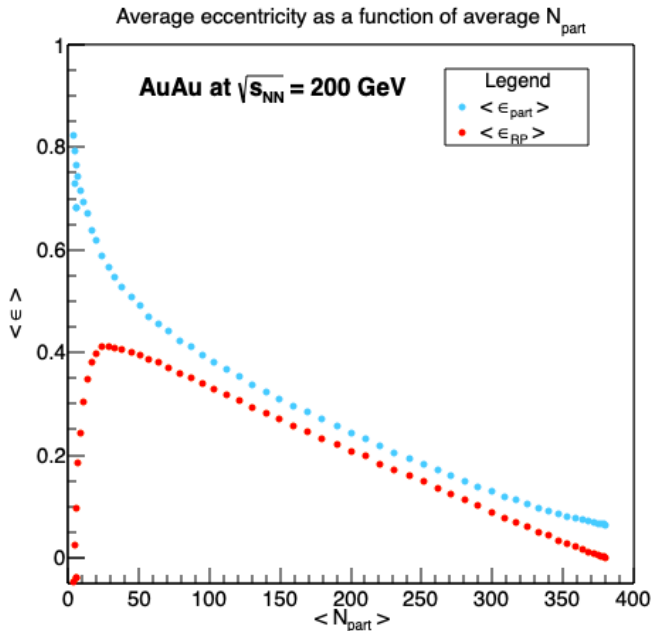

FIG. 14. Average reaction-plane and participant eccentricity as a function of the average N_{part} for Au+Au at 200 GeV.

Table I (pg. 11) shows the calculated eccentricities and overlap areas, in addition to the average impact parameter and average number of participants, for a variety of centrality classes. This table was meant to reproduce the values shown in a similar table (see Table II, pg. 11) in Hirano and Nara's paper. While the values do not perfectly agree, I can attribute any discrepancies to two main differences in methodology. First, Hirano and Nara assume a finite size profile for the nucleons (i.e. not a delta function), so their nuclear density function is not exactly a Woods-Saxon distribution and therefore they use different input parameter values. Specifically, for Au+Au, they use $\rho_0 = 0.1695$ fm^{-3}, $r_0 = 6.42$ fm and $a = 0.44$ fm, while my table was filled using $r_0 = 6.38$ fm and $a = 0.535$ fm (same ρ_0) [11]. Secondly, as theorists, the authors determined their centrality classes based on cuts in impact parameter and not particle multiplicity. This is not experimentally feasible because the offset between the nuclei in any collision is not controllable, nor is the impact parameter a quantity that can actually be measured. For the sake of being thorough, I did redo the calculations of the average values based on cuts in b instead of refMult, and the values were much closer—for exam-

ple, it brought the average N_{part} for the 60-70% centrality class down from 29 to 23 (compared to Hirano and Nara's value of 19)—so it is clear that the choice of centrality variable matters. The overestimation of the number of participants likely also relates to the lack of exclusion in my model; that is, when randomly distributing the nucleons, I do not check that each nucleon is initially at least 1 fm from the other constituents of the nucleus it belongs to thereby allowing the nucleons to be closer together and therefore more likely to interact. Even with those differences in the construction of our MCG models, the appropriate trends in the data are preserved; collisions at small impact parameter are associated with high N_{part}, large overlap areas, and small eccentricities, while less central collisions at large impact parameter have comparatively lower N_{part}, smaller overlap areas, and large eccentricities.

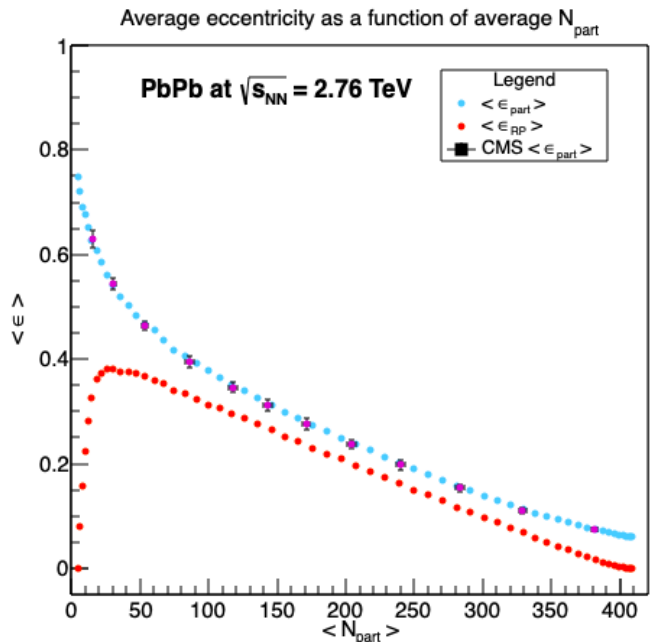### B. Pb+Pb at $\sqrt{s_{\text{NN}}} = 2.76$ TeV

FIG. 15. Average reaction-plane and participant eccentricity as a function of average N_{part} for Pb+Pb at 2.76 TeV.

As with the Au+Au collisions, the behavior of the average reaction-plane and participant eccentricities as functions of N_{part} is consistent with expectations, in this case from experimental data. In Fig. 15, the participant eccentricity value calculated using my MCG model (blue points) are clearly in good agreement with the CMS data (purple points with error bars) [12]. These experimentally-determined values are also listed in Table IV (pg. 11), which can be directly compared with the values in Table III of the average ϵ, S, b, and N_{part} for various centrality classes generated from my simula-

tion. The average number of participants is again being slightly overestimated, but the eccentricity and overlap area values still remain fairly consistent between the data and the model.
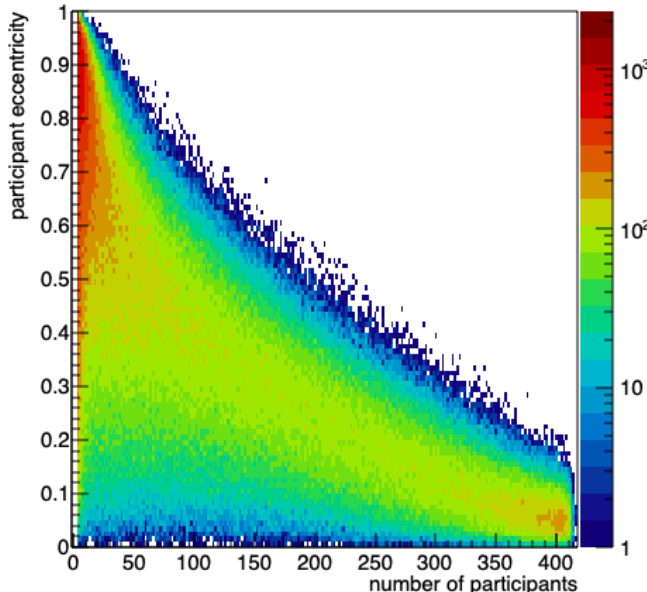

FIG. 16. Correlation between ϵ_{part} and N_{part}.

Fig. 16 shows the approximately negative correlation between the participant eccentricity and the number of participants for a given nucleus-nucleus collision. More importantly, the distribution of eccentricity values becomes much broader and more diffuse for low N_{part}. In those more peripheral events, fluctuations in the positions of the nucleons from event to event have a greater impact on the resulting calculation; furthermore, that demonstrates the need for Monte Carlo methods in these simulations, since only using the averages would not capture the entirety of the physics at work in these complicated processes.

V. CONCLUSIONS AND FUTURE WORK

The importance of knowing these geometric quantities, especially the eccentricity, comes from their relevance to elliptic flow analysis. The eccentricity characterizes the initial spatial anisotropy, which is responsible for the final anisotropy in the momentum distribution for the emitted charged particles. The transfer of anisotropy is studied as part of the collective flow of quarks and gluons observed in the dense medium produced in relativistic heavy ion collisions. This elliptic flow is quantified by its strength v_2, the second term in a Fourier expansion of the particles' invariant yield. This refers to the the integrated flow over a broad range of rapidity (i.e. the angular separation of the outgoing particles related to their relativistic motion) and transverse momentum [12]. Eccentricity calculations will be useful for characterizing the

various collision shapes across different event classes and for measurements of elliptic flow of heavy mesons. Quark flow has been observed for light quarks, but current experimentation is looking into whether heavy quarks undergo hydrodynamic flow as well. In both cases, elliptic flow reveals information about the initial conditions of the collision because it preserves the anisotropy. Knowing the eccentricity would also be useful for analysis of eccentricity-scaled elliptic flow, $v_2/\epsilon_{\text{part}}$; dividing v_2 by the eccentricity can potentially remove the dependence of the collective flow and the anisotropy parameter on the initial nucleus-nucleus collision area, thereby enabling better comparison of results across multiple centralities, colliding species, and center-of-mass energies.

Future work on this particular project involves the analysis of more datasets, specifically Pb+Pb at $\sqrt{s_{\text{NN}}} = 5.02$ TeV, to provide more values of ϵ for elliptic flow analysis. This phenomenon of elliptic flow is a crucial pillar of evidence for the formation of a quark-gluon plasma in experimental settings. Creating a QGP requires collisions between heavy ions moving at nearly the speed of light in order to reach the extreme temperature and density conditions seen in the very early universe. Continued study of the complex, high multiplicity nucleus-nucleus collisions occurring at the LHC and RHIC will provide further insights into the behavior of quantum chromodynamics and nuclear matter at high energies and into the state of matter in the first microseconds of the universe.

[1] M. Riordan and W. Zajc, "The first few microseconds", *Scientific American* (May, 2006) 34-41, `https://www.scientificamerican.com/article/the-first-few-microsecond-2006-05/`

[2] A. R. Kesich, "Upsilon Production and Suppression as Measured by STAR in $p+p$, $d+$Au, and Au$+$Au Collisions at $\sqrt{s_{\mathrm{NN}}} = 200$ GeV", UC Davis Ph.D Thesis (2014).

[3] R. Kunzig, "The Glue That Holds the World Together", *Discover* (Jul., 2000) 51-55, `https://discovermagazine.com/2000/jul/featgluons`

[4] B. Jacak and P. Steinberg, "Creating the perfect liquid in heavy-ion collisions", *Physics Today* **63** no. 5 (2010), `https://doi.org/10.1063/1.3431330`

[5] **CMS Collaboration**, "Measurement of nuclear modification factors $\Upsilon(1S)$, $\Upsilon(2S)$, and $\Upsilon(3S)$ mesons in PbPb collisions at $\sqrt{s_{\mathrm{NN}}} = 5.02$ TeV", *Physics Letters B* **790** (Mar., 2019) 270-293, `https://doi.org/10.1016/j.physletb.2019.01.006`

[6] CERN, "Heavy ions and quark-gluon plasma", `https://home.cern/science/physics/heavy-ions-and-quark-gluon-plasma`

[7] M. Anderson *et al.*, "The STAR Time Projection Chamber: A Unique Tool for Studying High Multiplicity Events at RHIC", *Nuclear Instruments and Methods in Physics Research Section A* **499** no. 2-3 (Mar., 2003) 659-678, `https://doi.org/10.1016/S0168-9002(02)01964-2`

[8] M. L. Miller, K. Reygers, S. J. Sanders, and P. Steinberg, "Glauber Modeling in High-Energy Nuclear Collisions", *Annual Review of Nuclear and Particle Science* **57** (May, 2007) 205-243, `https://www.annualreviews.org/doi/pdf/10.1146/annurev.nucl.57.090506.123020`

[9] M. Calderón de la Barca Sánchez. *Glauber Model + Particle Production Model*. Summer Research Program. Lecture conducted at the University of California - Davis (2017).

[10] **CMS Collaboration**, "Dependence on pseudorapidity and on centrality of charged hadron production in PbPb collisions at $\sqrt{s_{\mathrm{NN}}} = 2.76$ TeV", *Journal of High Energy Physics* (Oct., 2011), `https://arxiv.org/pdf/1107.4800`.

[11] T. Hirano and Y. Nara, "Eccentricity fluctuation effects on elliptic flow in relativistic heavy ion collisions", *Physical Review* **C79** (2009) 064904, `https://journals.aps.org/prc/abstract/10.1103/PhysRevC.79.064904`

[12] **CMS Collaboration**, "Measurement of the elliptic anisotropy of charged particles in PbPb collisions at $\sqrt{s_{\mathrm{NN}}} = 2.76$ TeV", *Physical Review C* (Jan., 2013), `https://arxiv.org/pdf/1204.1409`

TABLE I. Calculated eccentricities and overlap areas for a range of centrality classes (based on cuts in multiplicity) for Au+Au at $\sqrt{s_{NN}} = 200$ GeV. Except for the refMult ranges used to determine the centrality classes, all other reported values (b_{avg} through S_{part}) in the table are averages.

Centrality	0-5%	5-10%	10-15%	15-20%	20-30%	30-40%	40-50%	50-60%	60-70%
refMult	$\geq$566	447-566	353-447	278-353	168-278	97-168	52-97	26-52	13-26
b_{avg} (fm)	2.264	4.015	5.211	6.215	7.378	8.724	9.873	10.89	11.79
N_{part}	351.3	299.9	253.8	213.8	165.9	114.6	76.34	48.22	29.02
ϵ_{RP}	0.03181	0.09117	0.145	0.1915	0.2469	0.3094	0.3559	0.3816	0.3885
ϵ_{part}	0.08542	0.1311	0.1803	0.2269	0.2858	0.3598	0.4246	0.4873	0.557
S_{RP} (fm^2)	25.99	23.38	20.85	18.62	15.87	12.79	10.29	8.216	6.426
S_{part} (fm^2)	25.94	23.3	20.76	18.5	15.72	12.58	10.02	7.842	5.919

TABLE II. Average eccentricities, overlap areas, and number of participants for various centrality classes for Au+Au at $\sqrt{s_{NN}} = 200$ GeV, from T. Hirano and Y. Nara [11].

Centrality	0-5%	5-10%	10-15%	15-20%	20-30%	30-40%	40-50%	50-60%	60-70%
b_{min} (fm)	0.0	3.3	4.7	5.8	6.7	8.2	9.4	10.6	11.6
b_{max} (fm)	3.3	4.7	5.8	6.7	8.2	9.4	10.6	11.6	12.5
N_{part}	352	295	245	204	154	104	65.1	36.8	18.8
ϵ_{RP}	0.0446	0.120	0.183	0.233	0.292	0.348	0.389	0.405	0.398
ϵ_{part}	0.0818	0.145	0.204	0.254	0.318	0.380	0.433	0.473	0.497
S_{RP} (fm^2)	23.4	20.5	18.0	16.0	13.5	10.9	8.69	6.78	5.07
S_{part} (fm^2)	23.4	20.5	18.0	16.0	13.5	10.9	8.65	6.73	5.05

TABLE III. Calculated eccentricities and overlap area for a range of centrality classes (based on cuts in ΣE_T) for Pb+Pb at $\sqrt{s_{NN}} = 2.76$ TeV. Except for ΣE_T ranges used to designate the centrality classes, all other reported values are averages.

Centrality	0-5%	5-10%	10-15%	15-20%	20-25%	25-30%
ΣE_T (TeV)	$\geq$ 3.25	2.55-3.25	2.025-2.55	1.6-2.025	1.25-1.6	0.95-1.25
b_{avg} (fm)	2.322	4.142	5.403	6.39	7.25	8.041
N_{part}	377.2	333.6	286.1	245.1	208.8	175.7
ϵ_{RP}	0.01698	0.06296	0.1126	0.1558	0.1924	0.2278
ϵ_{part}	0.07506	0.1103	0.1535	0.1951	0.2335	0.2721
S_{RP} (fm^2)	29.12	26.71	24.1	21.76	19.67	17.71
S_{part} (fm^2)	29.07	26.63	24.0	21.64	19.52	17.54
Centrality	30-35%	35-40%	40-50%	50-60%	60-70%	70+%
ΣE_T (TeV)	0.75-0.95	0.55-0.75	0.3-0.55	0.15-0.3	0.1-0.15	<0.1
b_{avg} (fm)	8.718	9.355	10.24	11.3	12.06	14.12
N_{part}	148.4	124.1	92.72	60.53	41.38	12.6
ϵ_{RP}	0.2558	0.2821	0.3154	0.3433	0.3542	0.1753
ϵ_{part}	0.3047	0.3379	0.3857	0.4433	0.4916	0.6853
S_{RP} (fm^2)	16.06	14.51	12.41	10.02	8.345	3.669
S_{part} (fm^2)	15.85	14.28	12.12	9.636	7.869	3.376

TABLE IV. Average ϵ_{part}, S_{part}, and N_{part} for various centrality classes for Pb+Pb at $\sqrt{s_{NN}} = 2.76$ TeV [12].

Centrality	0-5%	5-10%	10-15%	15-20%	20-25%	25-30%
N_{part}	381$\pm$2	329$\pm$3	283$\pm$3	240$\pm$3	204$\pm$3	171$\pm$3
ϵ_{part}	0.074$\pm$0.003	0.111$\pm$0.005	0.154$\pm$0.007	0.198$\pm$0.009	0.238$\pm$0.009	0.276$\pm$0.010
S_{part} (fm^2)	29.4$\pm$1.2	26.6$\pm$1.1	24.0$\pm$1.0	21.6$\pm$1.0	19.5$\pm$0.9	17.5$\pm$0.8
Centrality	30-35%	35-40%	40-50%	50-60%	60-70%	70-80%
N_{part}	143$\pm$3	118$\pm$3	86.2$\pm$2.8	53.5$\pm$2.5	30.5$\pm$1.8	15.7$\pm$1.1
ϵ_{part}	0.312$\pm$0.011	0.346$\pm$0.010	0.395$\pm$0.010	0.465$\pm$0.008	0.543$\pm$0.011	0.630$\pm$0.016
S_{part} (fm^2)	15.7$\pm$0.8	14.1$\pm$0.7	12.0$\pm$0.6	9.4$\pm$0.5	7.1$\pm$0.4	4.8$\pm$0.3